Three-dimensional properties of Andes mountain waves observed by satellite: A case study

M. Joan Alexander[1] and Hector Teitelbaum[2]

[1]   The southern Andes region has been clearly identified in previous satellite and balloon observations and in global models as a "hot spot" of small-scale gravity wave activity, with monthly mean momentum fluxes exceeding 10 times background values in fall, winter, and spring seasons. This makes this region a focus of interest for global circulation and climate studies. We analyze a case study on 8 May 2006, combining observations from the Atmospheric Infrared Sounder instrument on the Aqua satellite and the High Resolution Dynamics Limb Sounder instrument of the Aura satellite to form a three-dimensional picture of the wave field. The observations show a widespread wave pattern over the southern Andes extending eastward over the south Atlantic. Simulations with the Weather Research Forecasting model clearly identify the waves as orographic in origin, but the observed wave pattern is far from the simple two-dimensional wave field forced by steady flow over a mountain ridge. The morphology of the pattern is consistent with three-dimensional linear theoretical calculations of downstream propagation and latitudinal focusing of mountain waves into the stratospheric jet. The observations confirm the importance of this process in the stratosphere, and we find the process also occurring in the global analysis and forecasts from the European Centre for Medium-Range Weather Forecasting. Our analysis evaluates some strengths and weaknesses of current orographic wave drag parameterizations in global models and the relevance of parameterization assumptions in global models with high resolution.

Citation: Alexander, M. J., and H. Teitelbaum (2011) Three-dimensional properties of Andes mountain waves observed by satellite: A case study, *J. Geophys. Res.*, *116*, D23110, doi:10.1029/2011JD016151.

1.   Introduction

[2]   Chemical and dynamical processes in the Southern Hemisphere stratosphere have well known effects on the development of the ozone hole and its predicted recovery in the 21st century. Recent research has also uncovered a relationship between stratospheric ozone recovery and projected changes in the seasonal cycle of surface winds in the Southern Hemisphere [*Perlwitz et al.*, 2008; *Son et al.*, 2008; *Turner et al.*, 2009]. Gravity wave drag in the high-latitude winter season stratosphere has a strong effect on the strength of vortex winds, vortex temperatures, and the depth and timing of the development of the ozone hole each year [e.g., *Austin and Wilson*, 2006; *Schmidt et al.*, 2006; *Alexander et al.*, 2010].

[3]   As early as 1996, space-based methods for detecting small-scale temperature fluctuations in the stratosphere identified the region over the southern Andes as a hot spot of small-scale wave activity [*Wu and Waters*, 1996; *Jiang et al.*, 2002; *Eckermann and Preusse*, 1999; *Wu and Eckermann*, 2008; *Wells et al.*, 2011]. More recently, methods for estimating gravity wave momentum flux globally also identified this region as an important source for waves contributing to drag on the Southern Hemisphere winds [*Ern et al.*, 2004; *Alexander et al.*, 2008; *Hertzog et al.*, 2008], confirming earlier model results [*Bacmeister*, 1993].

[4]   This paper describes an in depth case study of gravity waves in the stratosphere over the Southern Andes in this hot spot region. We present the three-dimensional structure of the wave field as observed from two satellite instruments: the Atmospheric Infrared Sounder (AIRS) instrument on the Aqua satellite and the High Resolution Dynamics Limb Sounder (HIRDLS) instrument on the Aura satellite. The case, on 8 May 2006, displays a morphology with short horizontal wavelength waves directly above and approximately aligned with the Andes ridge and longer horizontal wavelength waves downstream, with phase fronts aligned northwest to southeast.

[5]   A previous study using coarser-resolution satellite measurements observed some features of a similar downstream field and identified a southeastward group velocity for mountain waves in this region [*Preusse et al.*, 2002]. More recently, similar downstream propagation with focusing into the stratospheric jet was identified in a global gravity wave resolving model study [*Sato et al.*, 2011]. The downstream wave propagation was described with a three-dimensional

[1]NorthWest Research Associates, Boulder, Colorado, USA.
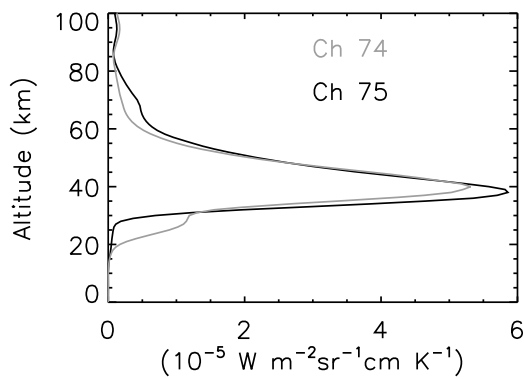[2]Laboratoire de Meteorologie Dynamique, Paris, France.

Figure 1. Temperature kernels for AIRS channels 74 and 75. The measured radiance at these channels is due to emissions from stratospheric altitudes, with the kernels peaking at 40 and 38 km, respectively.

linear, small-amplitude theory for mountain wave propagation. The southward and downstream propagation described in this *Sato et al.* [2011] study results when a component of the wave propagation vector is perpendicular to the wind vector. (Note the global model in the *Sato et al.* [2011] study did not resolve the shorter horizontal wavelength features we observe with AIRS directly above the Andes.)

[6] Here we compare the AIRS and HIRDLS satellite measurements to Weather Research Forecasting (WRF) model simulations of the 8 May 2006 case, and the comparison provides a validation of the gravity waves in the model. Close examination of the model further reveals nonlinearities in the wave field in the stratosphere that suggest some alteration of the simpler picture afforded by the linear theory. An analysis of the satellite data gives a measure of spatial variations of momentum flux across the wave pattern, and we contrast wave properties directly above the topography with those downstream. We also compare to the operational atmospheric data from the European Centre for Medium-Range Weather Forecasting (ECMWF), which in 2006 was provided at a resolution of T799 with 91 vertical levels. The results permit an observationally based case study estimation of the relative roles of smaller-scale parameterized and resolved waves that would be appropriate in a high-resolution global model.

2. Description of the Satellite Observations

[7] The AIRS instrument on the Aqua satellite and the HIRDLS instrument on Aura fly in formation in the international "A-Train" satellite constellation [*Schoeberl et al.*, 2004]. The A-Train satellites fly at high-inclination, with equatorial crossings at fixed local solar times of 1:30 am and 1:30 pm. Although the orbit tracks for AIRS-Aqua and HIRDLS-Aura are coincident, AIRS is a cross-track nadir scanning instrument while HIRDLS is a limb scanner with a line of sight azimuth angle of 47° to the anti-Sun side of the orbital plane [*Gille et al.*, 2008]. Thus instead of viewing the same geographical region nearly simultaneously with other A-Train instruments, the same location is viewed on a preceding or following orbit.

[8] AIRS observations of the southern Andes region on 8 May 2006 occur at approximately 05:45 UT and 19:15 UT.

HIRDLS views the same location at approximately 03:00 UT and 21:15 UT. Since mountain waves are approximately stationary and develop on timescales of hours to days, we neglect these minor differences in timing, but retain the AM/PM distinction. We will subsequently refer to these two events as 05:00 UT and 20:00 UT for the AM and PM observations, respectively. The AM/PM distinction will be shown to be important primarily because of differences in the HIRDLS viewing geometry in these two cases.

[9] For AIRS, we use radiance imagery of the 8 May event using two channels in the 15-μm emission band from CO_2 that peak in the stratosphere: Channels 74 (667.5 cm^{-1}) and 75 (667.8 cm^{-1}). Figure 1 shows the kernel functions for these channels for polar winter conditions [*Hoffmann and Alexander*, 2009]. The peaks lie at ~40 and 38 km, respectively. Radiance anomalies are computed as deviations from a fourth-order polynomial fit in the cross-track directions which effectively removes the scan angle dependence in the radiances. The background removal effectively filters waves with horizontal wavelengths longer than ~500 km. Brightness temperature anomalies are computed from radiance anomalies as described by *Alexander and Barnet* [2007] using a background temperature $\bar{T}$ = 235 K. AIRS observations give a horizontal plan view of brightness temperature perturbations over the region with a 13.5-km diameter horizontal footprint at the nadir, and an average footprint of ~20 km diameter. The imagery represent an integrated measurement in height, as described by the kernel functions in Figure 1, which would effectively eliminate any short vertical wavelength waves. The fast eastward wind speeds in the stratosphere lead to refraction of the mountain waves to long vertical wavelengths that can survive this vertical integration.

[10] HIRDLS, conversely, gives cross sections of temperature perturbation with fine vertical resolution. The instrument field of view projected onto the limb has a vertical width of 1.2 km, and the HIRDLS temperature retrievals can effectively resolve waves with vertical wavelengths as short as 4 km [*Alexander and Ortland*, 2010]. The horizontal resolution along the measurement track is determined by the spacing between vertical profiles, which is ~100 km. Along the line of sight, the limb measurement represents an integral with the typical horizontal length of ~150 km. Short horizontal wavelength waves with phase fronts perpendicular to the line of sight will therefore be effectively filtered from the HIRDLS measurements, while if their phase fronts are parallel to the line of sight they can be observed, but undersampled [e.g., *Eckermann and Preusse*, 1999].

[11] HIRDLS gravity wave perturbations are computed here as temperature anomalies from the large scale. The large scale is defined as the zonal mean plus planetary scale waves with zonal wave numbers 1–3 [*Alexander et al.*, 2008].

3. WRF Model Description

[12] Weather Research Forecasting model (WRF [*Skamarock et al.*, 2005]) simulations are configured to investigate whether the waves seen in the satellite data are orographic waves. WRF is run in a nested configuration covering the Southern Andes region. An outer domain has horizontal resolution 21-km and 2000 × 2000 km^2 area, and an inner domain with 7-km resolution and 700 × 700 km^2
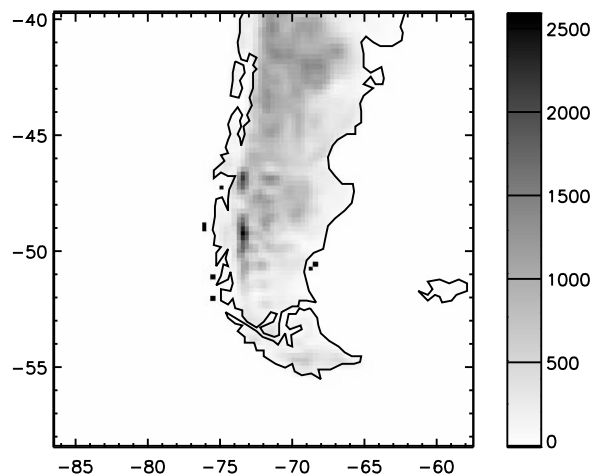
Figure 2. Topography (m) of the southern Andes mountains shown at resolution of the outer WRF model domain.

area over the Andes topography is centered within. The model extends from the surface to 45 km in the vertical with 115 levels. We include a sponge layer above 40 km to limit wave reflection from the top boundary. Vertical resolution increases from 0.2 km at low levels to 0.6 km at 30 km altitude, then further increases to 2 km in the sponge layer. The model is initialized at 00:00 UT on 7 May with ECMWF analysis fields and the analysis defines conditions at the outer boundaries of the large domain throughout the simulation. We also initiated another run at 00:00 UT on 8 May to examine any influence of incomplete absorption in the sponge layer on the solutions. This comparison shows some wave reflection from the top boundary appearing as weak perturbations on the observed wave pattern, although the slower, longer waves in the field do not have sufficient time to fully develop at the satellite observation level in this case, so we do not examine this simulation further.

[13] Topography on the 21-km domain grid is shown in Figure 2. The zonal wind upstream of the topography is shown in Figure 3. Low-level upstream winds are southeastward with speeds up to 30 m s^{-1} and peaking at latitudes with the highest terrain. Winds in the stratosphere are primarily zonal and reach 55 m s^{-1} near 40 km altitude. Within the model domain (40–60°S), the jet in the stratosphere increases gradually with increasing southern latitude. The model includes microphysics using the Thompson scheme [*Thompson et al.*, 2004], but moist processes are rather unimportant in this case study. Only very light rain occurs along the coast west of the mountains, accumulations less than 2.5 mm in the 4 h from 0 to 04:00 UT on 8 May. These are small values that are unlikely to be involved in wave forcing in any significant way. A second simulation with the same configuration, except without the mountains, is also performed for comparison.

4. Model Comparison to Observations

[14] The AIRS channel brightness temperature anomalies (T_B') for the AM (05:00 UT) and PM (20:00 UT) overpasses are shown in Figure 4, as the average of channels 74 and 75. Only perturbations with $|T_B'| > 0.4$K, which is 3 times the estimated noise, are colored. These are otherwise raw,

unsmoothed, unfiltered data. Bands of alternating positive and negative T_B' can be seen running roughly parallel to the west coastal outline and downstream between ~45° and 50°S latitude, and further north to 40°S in the PM case. These features have short horizontal wavelengths <100 km, approaching the AIRS resolution limits. Extending from these to the south and east are longer horizontal wavelength features, which extend out over the sea well beyond any topography. These qualitatively resemble the topographic waves observed to propagate downstream and southward, focusing in the stratospheric jet to the south and east of the Andes topography, in the global simulations reported by *Sato et al.* [2011]. The wave field is observed to be approximately stationary during the 15 h interval separating the AM and PM overpasses.

[15] Figure 5 shows temperatures at 40 km altitude in the WRF simulation at 05:00 UT and 20:00 UT for comparison to the AIRS observations. The observed wave pattern is well reproduced in the simulation, including the pattern location, wave orientation, and horizontal wavelengths. The largest amplitude shorter horizontal wavelength waves are observed parallel to and in the lee of the main Andes ridge. Weaker longer horizontal wavelength waves are also observed to extend to the south and east over the south Atlantic Ocean with similar orientation as those in the observations. Locations of HIRDLS profiles along the HIRDLS measurement track are overplotted on these maps with black circles.

[16] Figure 6 shows profiles of the HIRDLS gravity wave temperature anomalies arranged in sequence to show a longitude-height cross section along the line formed by the measurement track for both the AM (05:00 UT) and PM (20:00 UT) overpasses. For comparison, Figure 7 shows vertical cross sections of the model sampled along the HIRDLS measurement track. Model temperatures here are shown as perturbations from the trend along the section computed at each altitude. Comparison of Figures 6 and 7 show close quantitative agreement between the gravity
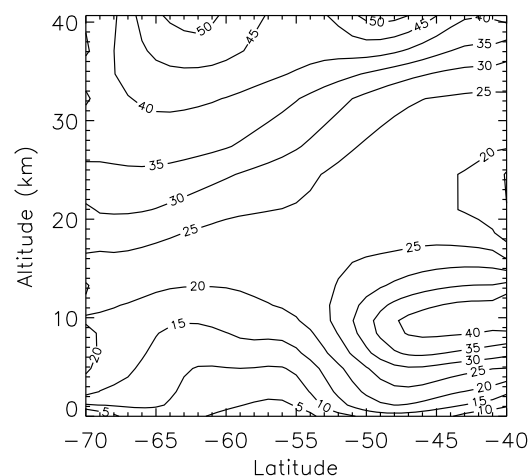

Figure 3. Upstream zonal wind (contours every 5 m s^{-1}), averaged between 80 and 100° W longitude, on 8 May versus latitude and height from the 06:00 UT ECMWF analysis. Eastward surface winds maximize between 45 and 50°S and stratospheric vortex winds exceed 50 m s^{-1} between 60 and 65°S.
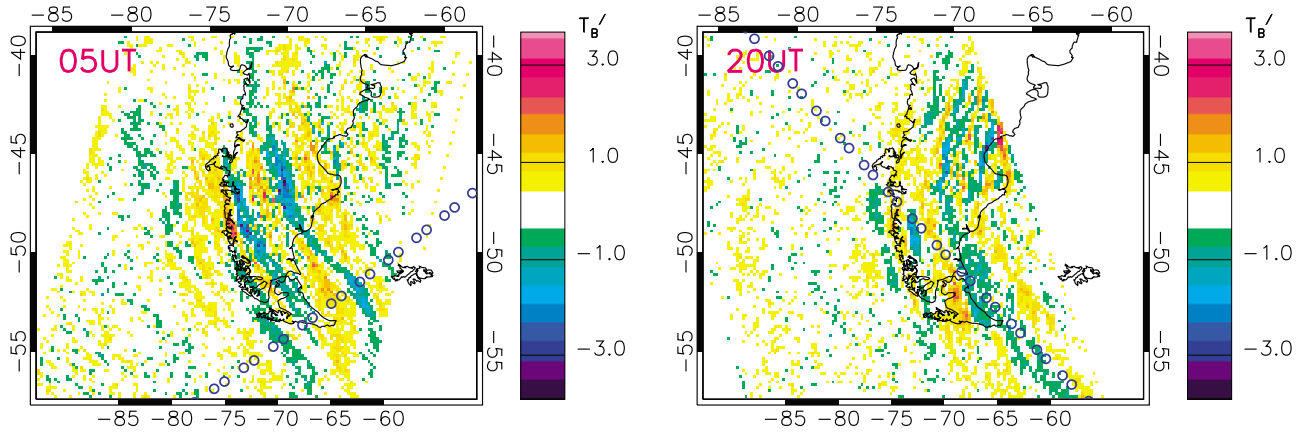
Figure 4. Waves at 05:00 UT and 20:00 UT shown as the average of brightness temperature anomalies in AIRS channels 74 and 75. Blue circles mark the locations of corresponding AM and PM HIRDLS profiles.

waves observed by HIRDLS and those in the simulation. The model naturally shows details in the horizontal structure that are undersampled by the HIRDLS measurements. Aside from these resolution differences, the modeled and observed cross sections show nearly feature-for-feature matching. Differences appear in the 05:00 UT case where HIRDLS resolution is only barely resolving the short-horizontal wavelength structure seen at altitudes between ~30 and 40 km. The 20:00 UT comparison also shows even finer structure in the model at −75° to −72° longitude that is absent in the HIRDLS cross section, and some differences are also seen in the −65° to −60° region where the apparent horizontal wavelength is longer in the model than in the observations. This latter difference is likely indicating some difference in the horizontal orientation of the phase lines that can also be seen in the AIRS comparison. The good quantitative agreement between HIRDLS and the model is in part due to the favorable orientation of the HIRDLS line of sight, which coincidentally falls

approximately along the lines of constant phase in the wave field for both the AM and PM overpasses.

[17] These comparisons provide a very good validation of the three-dimensional structure of the gravity waves in the simulation. With the model, we can investigate further to examine the nature of the wave source and any nonlinearities occurring within the wave field in the stratosphere.

[18] Figure 8 compares the wave field in the WRF simulation and a second simulation with orographic relief set to zero. Note the complete absence of the waves directly above the topography in the second simulation, and only extremely weak northwest to southeast oriented waves across the domain that are a factor of 10 weaker than in the simulation with topography, lending further evidence that the waves seen in the satellite observations are orographic in origin. Weak NW-SE trending wave features are common at this latitude and altitude in gravity-wave resolving models [*Wu and Eckermann*, 2008] and are likely related to jet stream imbalance. Their orientation is likely also associated with
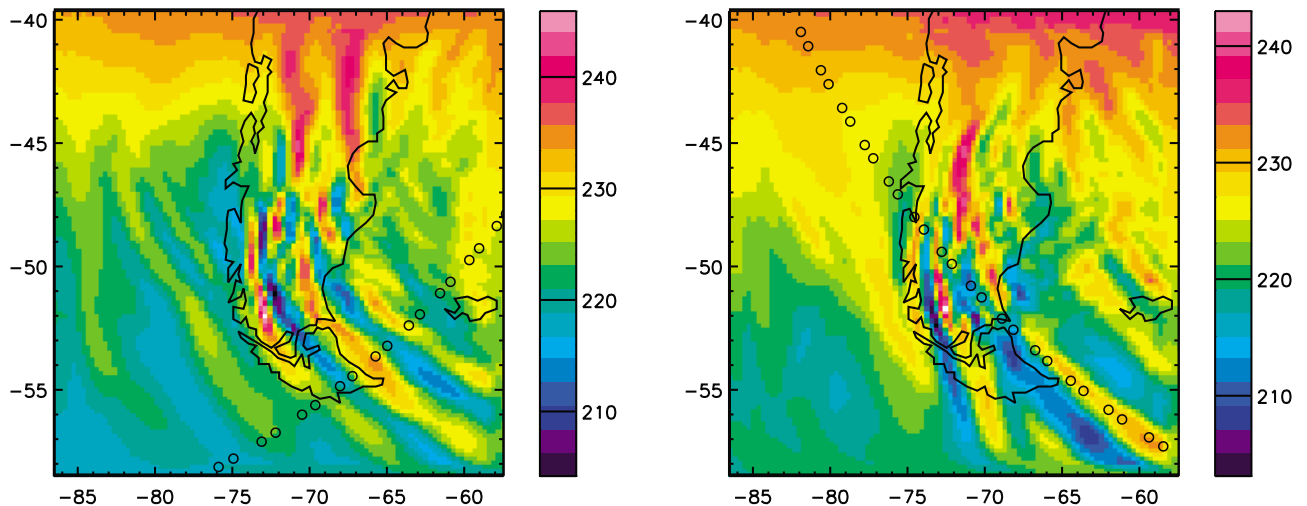

Figure 5. Model temperatures at 05:00 UT and 20:00 UT at 40-km altitude on the WRF outer domain grid. Black circles mark the locations of HIRDLS profiles as described in the text.
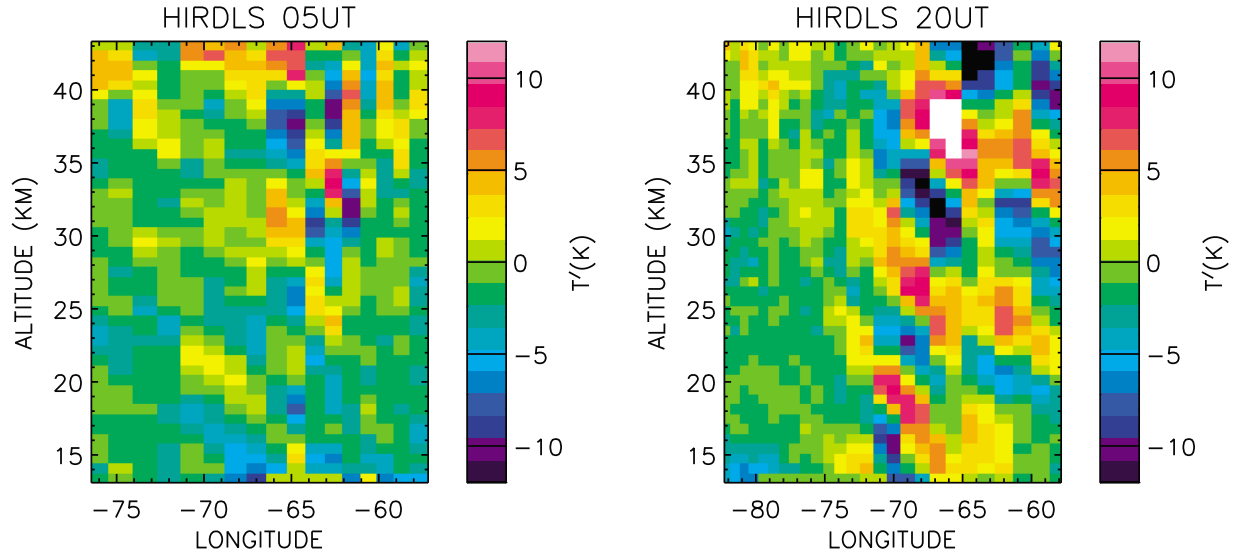
Figure 6. Wave temperature anomalies at 05:00 UT and 20:00 UT observed by HIRDLS plotted as vertical cross sections along the HIRDLS measurement track.

the wind focusing effect on wave propagation described by *Sato et al.* [2011].

5. Analysis of the Wave Properties

[19] To evaluate the observed orographic wave effects on the circulation, the AIRS data are analyzed to estimate momentum fluxes. The analysis method, described by *Alexander et al.* [2009], computes spatially resolved features of the gravity wave field, including horizontal wavelength, propagation direction, and temperature amplitude. The horizontal wavelengths are computed from a wavelet analysis that includes wavelet cospectral variance of adjacent rows to determine the slopes of the features and hence the propagation direction. (Further details of the wavelet analysis are described by *Alexander and Barnet* [2007].) Vertical

wavelength and momentum flux are also computed by assuming that the waves are stationary and propagating upstream against the background wind.

[20] Briefly summarizing the *Alexander et al.* [2009] method, the momentum flux F is estimated from

$$F = \frac{\bar{\rho}}{2} \left(\frac{\lambda_z}{\lambda_H} \right) \left(\frac{g}{N} \right)^2 \left(\frac{\hat{T}}{\bar{T}} \right)^2 \tag{1}$$

where $\bar{\rho}$ is background density, λ_z and λ_H are the vertical and horizontal wavelengths, g is the gravitational acceleration, N the buoyancy frequency, and $\bar{T}$ the background temperature. $\hat{T}$ is the sensible temperature amplitude, which is related to the brightness temperature amplitude $\hat{T}_B$ by an amplitude correction factor $A(\lambda_z)$ that varies between 0
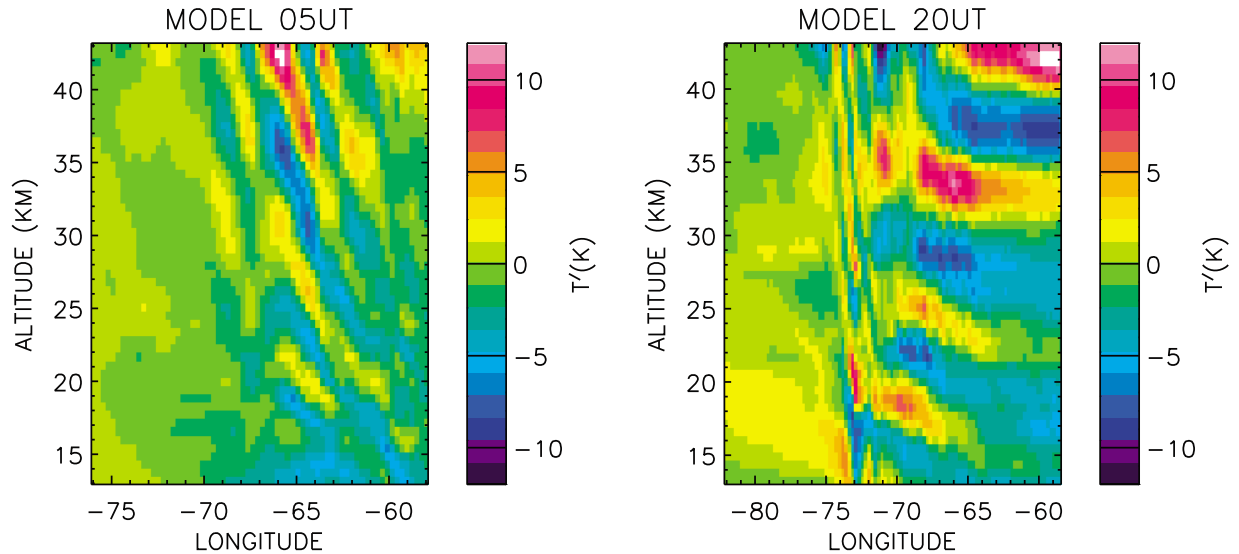

Figure 7. Wave temperature anomalies in the model at 05:00 UT and 20:00 UT plotted in cross section along the HIRDLS measurement track.
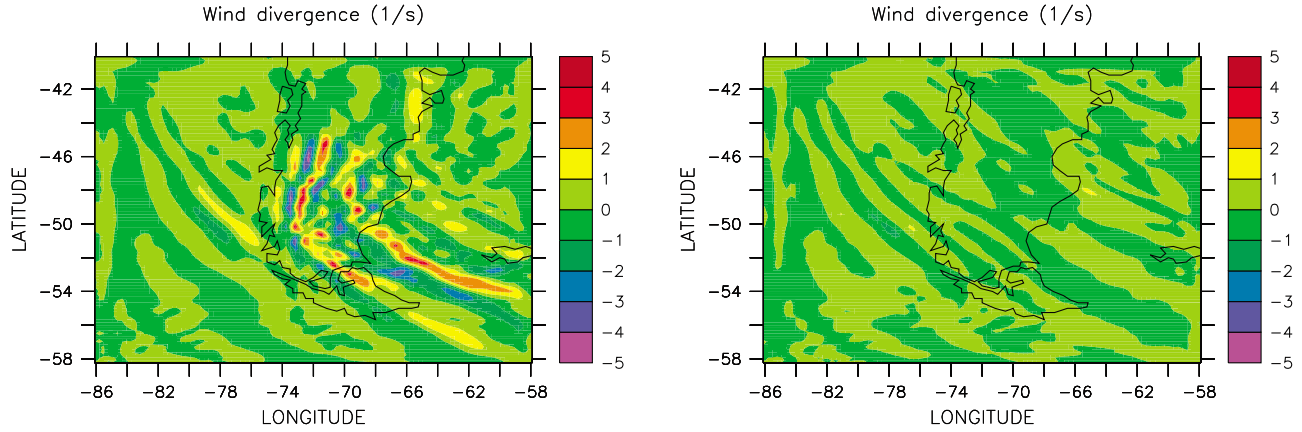
Figure 8. Horizontal wind divergence at 05:00 UT and 27-km altitude for the simulation (left) with and (right) without mountains.

and 1 with vertical wavelength according to the radiative transfer of the measurement as described by *Hoffmann and Alexander* [2009]:

$$\hat{T} = \hat{T}_B [A(\lambda_z)]^{-1} \qquad (2)$$

λ_z is not directly observed but is instead calculated from the dispersion relation:

$$\lambda_Z = 2\pi \left(\frac{N^2}{U_H^2} - k_H^2 \right)^{-1/2} \qquad (3)$$

where $U_H = \vec{k} \cdot \vec{U}/k_H$ is the horizontal wind in the direction of wave propagation and $k_H = |\vec{k}| = 2\pi/\lambda_H$ is the magnitude of the horizontal wave number. Spatially smoothed winds and static stability from the ECMWF analysis are utilized for this purpose. The factor A goes to zero at $\lambda_z \sim 12$km, and shorter vertical wavelengths are invisible to AIRS. Following *Alexander et al.* [2009], we only perform the calculation where the λ_z is longer than this limit to avoid any possibility of applying our stationary wave assumption to a nonstationary wave that might appear somewhere in the field of view of AIRS. We limit the analysis to $\lambda_z > 13$km where A in the denominator becomes very small to avoid the limit where the signals become too difficult to distinguish from noise.

[21] Figure 9 shows maps of the magnitude of momentum flux, horizontal wavelength, and vertical wavelength that have been binned in $0.5° \times 0.5°$ longitude-latitude bins and averaged over both AM and PM overpasses. Error in these fluxes, estimated as the standard deviation in a region north and upstream of the topography where no orographic waves are expected, is ±21 mPa. The results show that the waves observed close to the Andes mountain ridge between $\sim -50°$ and $-40°$ latitude tend to have different properties than the waves further to the south and downstream of the mountains. Table 1 summarizes these results. The waves over the mountains have shorter horizontal wavelengths, westward propagation directions, longer vertical wavelengths, and larger momentum fluxes. These properties are consistent with the hypothesis that the waves observed downstream and to the south extending out over the ocean are the larger-scale component of the mountain waves with group speed to the south and east from their origin over the Andes. These waves carry significantly less momentum flux than the waves observed over the topography because they have longer horizontal scales and phase orientation that is more parallel to the eastward winds. The vertical wavelengths of the waves near the southern end of the pattern visible in the AIRS images (Figure 4) are becoming shorter with increasing latitude, and as they shrink to <14 km, they begin to disappear due to the filtering affect of the AIRS kernel
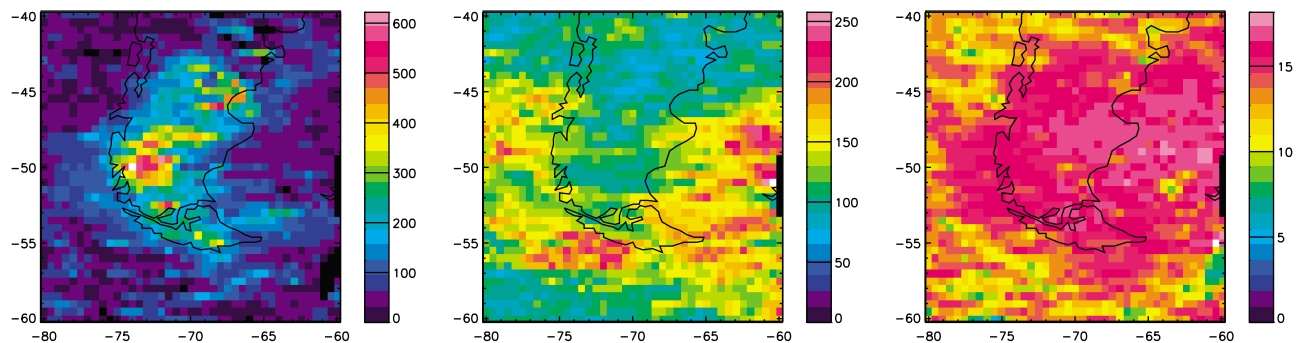

Figure 9. Results of the AIRS imagery analysis plotted versus longitude and latitude, showing (left) momentum flux (mPa), (center) horizontal wavelength (km), and (right) vertical wavelength (km).

Table 1. Wave Properties Estimated From AIRS Observations

Region	Average Flux	Vertical Wavelength	Horizontal Wavelength
75–71W, 52–48S	341 mPa	15.8 km	114 km
67–63W, 58–54S	103 mPa	14.8 km	156 km

function (Figure 1). The wave pattern therefore likely extends further to the south and east than we can see with AIRS but the vertical wavelength is too short. This is confirmed in the cross sections of HIRDLS observations and the WRF model (Figures 6 and 7).

6.   Origin of the Waves Over the Sea

[22]   The wave pattern observed to extend southward and downstream of the mountains in both the satellite observations and the model also appear in the operational ECMWF atmospheric data. At this time (in 2006), the ECMWF produced operational data at horizontal resolution T799 (grid spacing $\Delta \sim 25$ km) [*Orr et al.*, 2010]. After accounting for dissipation at the short scales, the shortest resolved waves at this resolution will occur with horizontal wavelengths $\sim 10\Delta \sim 250$ km [e.g., *Shutts and Vosper*, 2011]. Figure 10 shows ECMWF temperatures at 40 km altitude in this region along with the locations of the HIRDLS profiles to provide a location reference. We note that similar features appear at both forecast and analysis times in ECMWF, and they are likely caused by winds interacting with the resolved Andes topography in the model solutions, and not dependent on observations at the assimilation step [see, e.g., *Wu and Eckermann*, 2008].

[23]   The wave pattern extends down to the surface and is clearly tied to orography with cold anomalies on the upwind side of the mountains and warm anomalies on the leeward side. The horizontal wavelengths in ECMWF, are longer than in the observations, (~400 km), but near the smallest scale of resolved waves at the ECMWF resolution. The satellite observations and WRF simulation both suggest that the

waves immediately above the mountains likely have horizontal wavelengths too short to be resolved with the relatively coarse resolution of the ECMWF model. However, a long horizontal wavelength component of the mountain wave signal is clearly well represented. These long wavelength waves are most strongly advected downstream and southward via the mechanism described by *Preusse et al.* [2002] and *Sato et al.* [2011].

[24]   The model used in the ECMWF analysis includes a parameterization for orographic gravity wave drag [*Lott and Miller*, 1997]. Such parameterizations assume waves propagate purely vertically, and when they break they provide a drag force in the atmosphere directly over the topography. These assumptions are more nearly correct for the smallest-scale waves above the Andes seen in the AIRS data, and these short waves are not resolved in the ECMWF. Hence despite the fact that the long-wavelength features appearing downstream are resolved orographic waves in ECMWF, the short-wavelength features directly above the topography remain unresolved, and the AIRS analysis shows they carry several times more momentum flux than the resolved features. The short wave characteristics are qualitatively well described by the assumptions in the parameterizations. Therefore, despite the fact that some orographic gravity waves are resolved in ECMWF, this study suggests there remains good justification for continuing to employ orographic gravity wave drag parameterizations in the ECMWF model at this resolution.

7.   Mountain Wave Breaking

[25]   The high-resolution nested region of the simulation shows evidence that the waves are convectively unstable and that breaking or dissipation is important in the lower stratosphere. Figure 11 shows an example profile of potential temperature at 72.5W, 48S where the waves produce convectively unstable regions, here visible at 23–35 km altitude. Analysis of the wind profiles at this location (Figure 12) show that there is wave dissipation with an increase in amplitude up to this height, and a decrease in amplitude above. This is a common occurrence in the model, and Figure 13 shows the locations
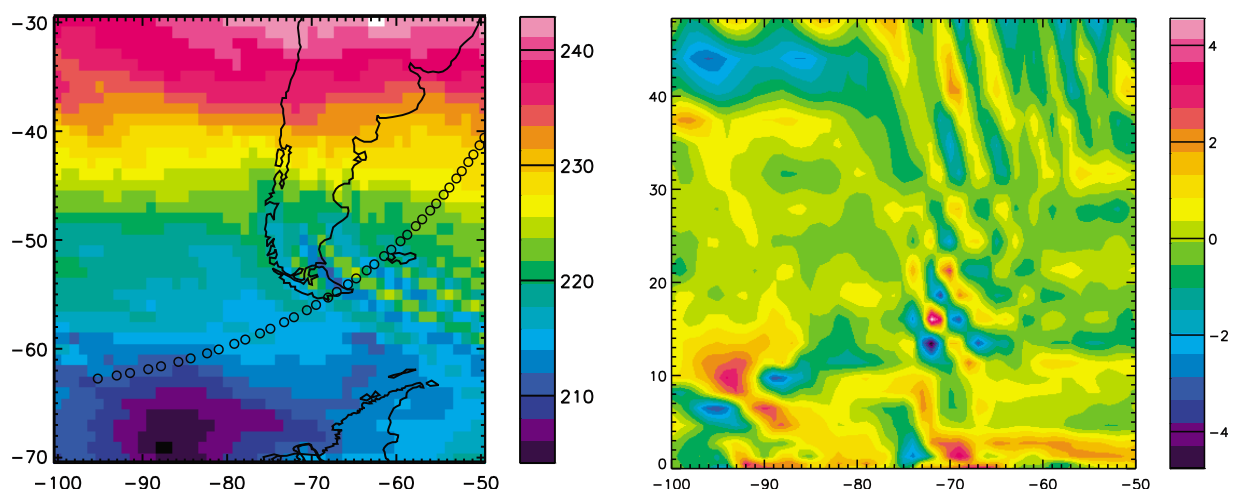

Figure 10.   (left) ECMWF temperatures (K) at 06:00 UT and 40-km altitude. Black circles again mark the locations of the HIRDLS profiles for reference. (right) Cross section of ECMWF temperature perturbations (K) at −49° latitude.
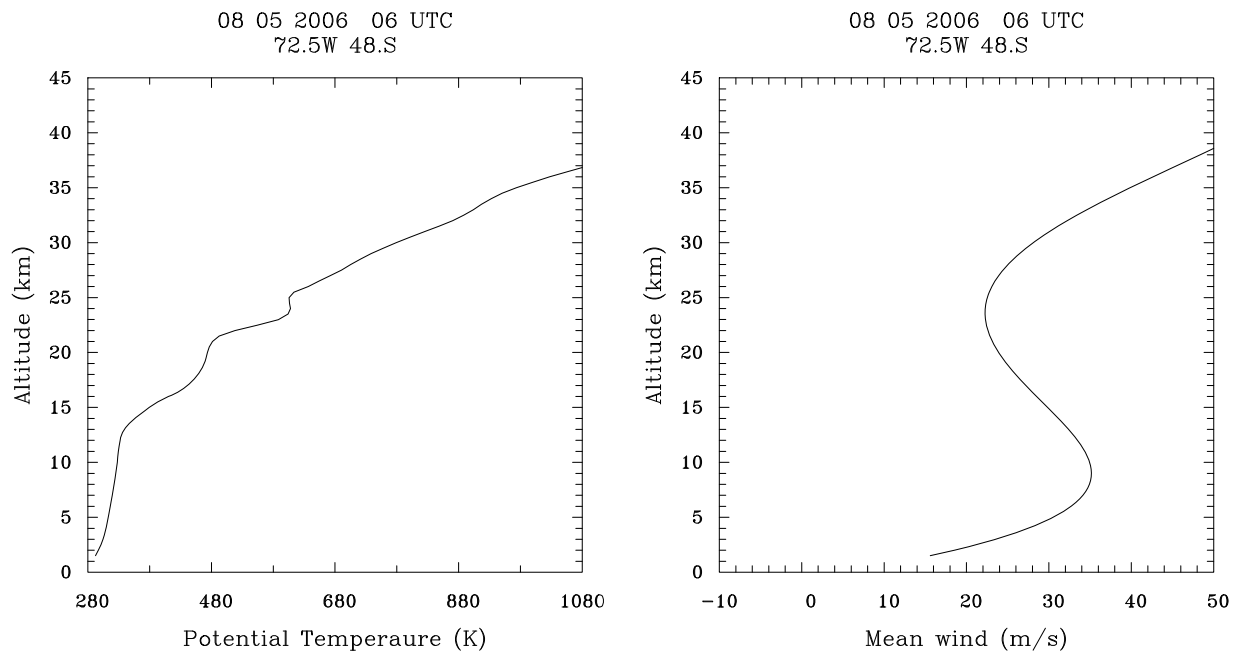
08 05 2006 06 UTC
72.5W 48.S

08 05 2006 06 UTC
72.5W 48.S

Figure 11. Example profiles at 72.5°W, 48.0°S at 06:00 UT from the high-resolution inner nested region of the WRF simulation, showing (left) potential temperature and (right) mean wind along the wave propagation direction (−15° south of east).

(green dots) of convectively unstable profiles (negative potential temperature gradients) found in the model between altitudes 12–25 km at 06:00 UT. Note that the strongest observed fluxes at 40 km (Figure 9) occur above this region, supporting the idea that wave breaking below does not completely eliminate mountain wave fluxes but only reduces them, qualitatively

analogous to the "wave saturation" assumptions commonly applied in orographic gravity wave drag parameterizations.

[26] The HIRDLS cross sections are not ideally oriented to evaluate the change in the mountain wave amplitudes with height, but they suggest growth in amplitude with altitude that is much slower between $z = 20$ and 40 km than that
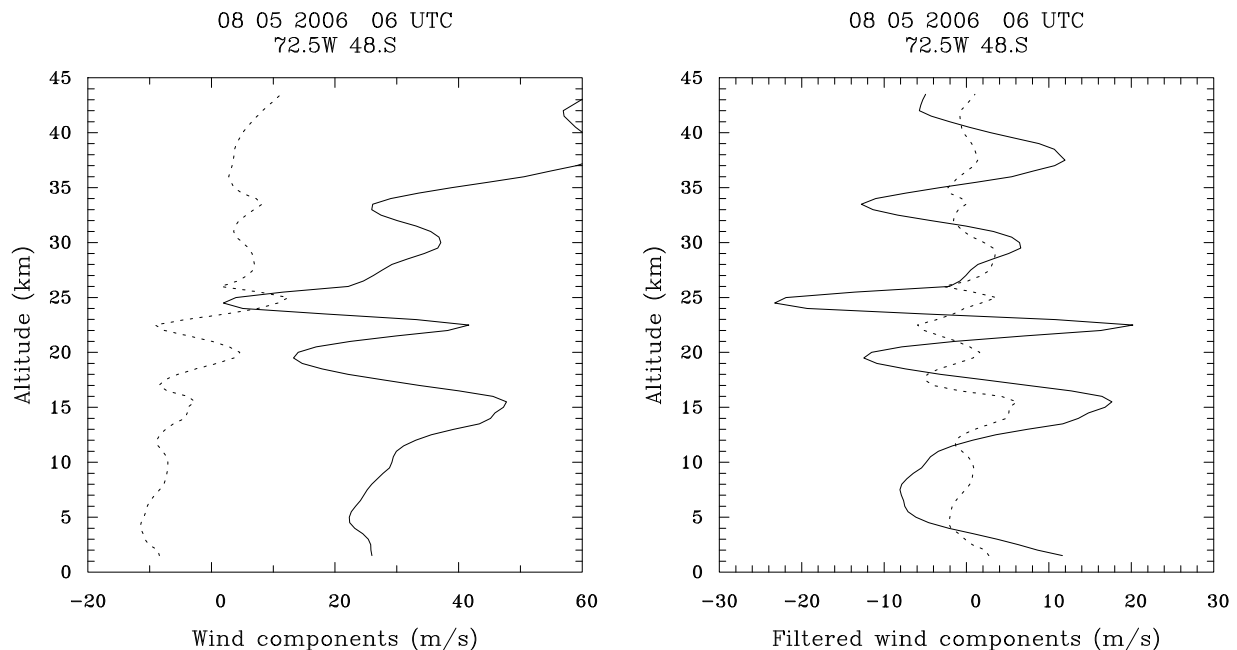
08 05 2006 06 UTC
72.5W 48.S

08 05 2006 06 UTC
72.5W 48.S

Figure 12. Wind profiles in the region of wave breaking, 72.5°W, 48.0°S at 06:00 UT from the inner nest of the WRF simulation, showing (left) zonal (solid) and meridional (dotted) winds and (right) perturbation winds along the propagation direction of the wave (solid) and perpendicular (dotted). The propagation is in the direction −15° south of east in this example.
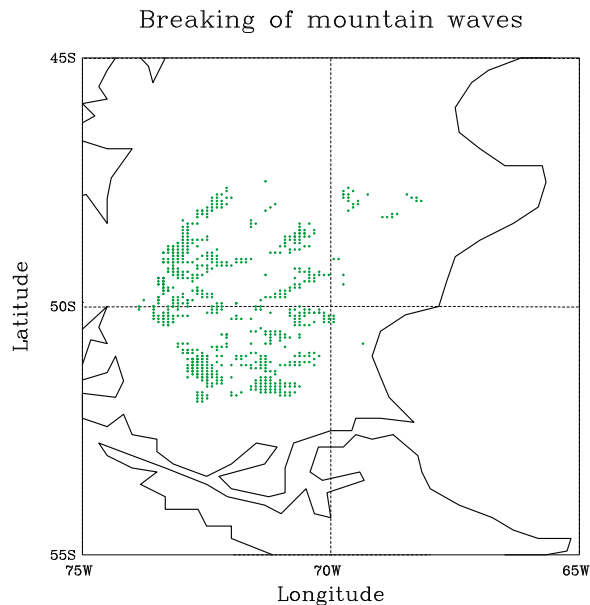
Figure 13. Map of the locations of wave breaking in the model at 06:00 UT. Breaking occurs between altitudes 12–25 km where the zonal winds are generally weak. The vertical wavelength of mountain waves with approximately zonal orientation reaches a minimum value there.

expected for linear waves. Linear wave growth in amplitude would be proportional to the inverse of the square root of density, $\bar{\rho}^{-1/2} \sim e^{z/2H} \sim 4$ growth factor over this altitude range, whereas the observations show only weak growth of a factor ~1.4. This weaker growth implies wave dissipation between 20 and 40 km and a westward drag force on the mean flow. With only four HIRDLS profiles in this region, we cannot estimate the change in amplitude with sufficient accuracy to estimate the force on the mean flow. However, the first row of Table 1 provides an estimate of momentum flux and horizontal wavelength in a $4° \times 4°$ area over the Andes that could be compared to parameterized flux in orographic gravity wave drag parameterizations on this day.

8. Summary and Conclusions

[27] AIRS and HIRDLS are shown to sample the same mountain wave event over the southern Andes where vertical wavelengths are long enough to be resolved by AIRS. The observed pattern closely resembles waves generated in a WRF model simulation sampled at horizontal resolution of 21 km. Note that 21 km is the resolution of the WRF outer domain grid, while an inner nest at 7 km was used in the mountain areas, and this finer resolution is likely important for modeling sufficient orographic relief to obtain the correct wave amplitudes. The wave pattern extends far out over the ocean to the south and east of the topography, and a second simulation without topography confirms the topographic origin of the waves. A wavelet analysis of the AIRS observations reveals the spatial distributions of horizontal wavelengths, propagation directions, and temperature amplitudes at 40 km altitude. With the results of this analysis, and with the assumption that the waves in the AIRS images

are stationary mountain waves, we further compute spatial patterns in momentum flux and vertical wavelength. The results confirm changes in the horizontal wavelengths with distance from the Andes topography that is visible by eye from inspection of the AIRS images, where the shortest waves are observed most directly above the topography with orientations approximately parallel to the mountain ridge, while the waves extending south and east over the ocean have longer horizontal wavelengths and southwestward propagation relative to the wind. The momentum flux associated with the short waves directly over the topography is also much larger than the flux associated with the long-wave component that extends out over the ocean. Further, the short-wave momentum flux is more nearly due westward while the long-wave flux is southwestward. This will tend to make the drag force on the zonal flow associated with the short waves even more important.

[28] The ECMWF analysis product contains a mountain wave pattern that resembles the long-wave component seen by the satellites, although the wavelength is longer than observed. The short waves directly above the topography are absent in the ECMWF result. This pattern of long waves extending out over the ocean is the most obvious three-dimensional propagation effect we see in the data. Theoretical calculations show that such three-dimensional propagation effects are exaggerated for longer horizontal wavelength waves and are relatively small for shorter horizontal wavelength waves [*Preusse et al.*, 2002; *Wells et al.*, 2011].

[29] Taken at face value, this implies two things: (1) At T799 resolution, the ECMWF fields well characterize the most obvious three-dimensional propagation effects of mountain waves. (2) Although the large-scale component of the mountain waves can be resolved in high-resolution global models, the shorter-wavelength waves that appear more directly above the topography are not resolved, and these short waves are associated with much larger zonal momentum fluxes than the long waves, so parameterization of this component is still appropriate. The short waves also display propagation that is more nearly two-dimensional, so more closely matches the assumption used in orographic gravity wave parameterizations. These parameterizations may thus be considered a still important and reasonably realistic way to treat the short-scale mountain waves in global models with similar resolution.

[30] We also estimate the orographic wave momentum flux in the region 71–74°W and 52–48°S to be 341 ± 21 mPa at 40 km altitude on this day. HIRDLS temperatures (four profiles) in this region and the WRF model results both suggest wave dissipation and a westward drag force on the mean flow in the lower stratosphere between 20 and 40 km altitude. The WRF model in particular suggests the force may be more localized in altitude between ~12 and 25 km. The uncertainties in the change in amplitude of the waves with height due to the limited number of HIRDLS profiles does not allow a meaningful estimate of the force, however the momentum fluxes at $z = 40$ km represent a quantitative result for 8 May 2006 that could be compared to results from an orographic gravity wave parameterization. Although a single comparison may not be definitive, similar comparisons on a collection of mountain wave events could provide important constraints for these parameterizations.

References

Alexander, M. J., and C. Barnet (2007), Using satellite observations to constrain gravity wave parameterizations for global models, *J. Atmos. Sci.*, *64*(5), 1652–1665.

Alexander, M. J., and D. A. Ortland (2010), Equatorial waves in High Resolution Dynamics Limb Sounder (HIRDLS) data, *J. Geophys. Res.*, *115*, D24111, doi:10.1029/2010JD014782.

Alexander, M. J., et al. (2008), Global estimates of gravity wave momentum flux from High Resolution Dynamics Limb Sounder (HIRDLS) observations, *J. Geophys. Res.*, *113*, D15S18, doi:10.1029/2007JD008807.

Alexander, M. J., S. D. Eckermann, D. Broutman, and J. Ma (2009), Momentum flux estimates for South Georgia island mountain waves in the stratosphere observed via satellite, *Geophys. Res. Lett.*, *36*, L12816, doi:10.1029/2009GL038587.

Alexander, M. J., et al. (2010), Recent developments in gravity wave effects in climate models, and the global distribution of gravity wave momentum flux from observations and models, *Q. J. R. Meteorol. Soc.*, *136*, 1103–1124, doi:10.1002/qj.637.

Austin, J., and R. J. Wilson (2006), Ensemble simulations of the decline and recovery of stratospheric ozone, *J. Geophys. Res.*, *111*, D16314, doi:10.1029/2005JD006907.

Bacmeister, J. T. (1993), Mountain-wave drag in the stratosphere and mesosphere inferred from observed winds and a simple mountain-wave parameterization scheme, *J. Atmos. Sci.*, *50*, 377–399.

Eckermann, S. D., and P. Preusse (1999), Global measurements of stratospheric mountain waves from space, *Science*, *286*(5444), 1534–1537.

Ern, M., P. Preusse, M. J. Alexander, and C. D. Warner (2004), Absolute values of gravity wave momentum flux derived from satellite data, *J. Geophys. Res.*, *109*, D20103, doi:10.1029/2004JD004752.

Gille, J. C., et al. (2008), The High Resolution Dynamics Limb Sounder (HIRDLS): Experiment overview, recovery and validation of initial temperature data, *J. Geophys. Res.*, *113*, D16S43, doi:10.1029/2007JD008824.

Hertzog, A., G. Boccara, R. A. Vincent, F. Vial, and P. Cocquerez (2008), Estimation of gravity wave momentum flux and phase speeds from quasi-Lagrangian stratospheric balloon flights. Part II: Results from the Vorcore campaign in Antarctica, *J. Atmos. Sci.*, *65*, 3056–3070, doi:10.1175/2008JAS2710.1.

Hoffmann, L., and M. J. Alexander (2009), Retrieval of stratospheric temperatures from AIRS radiance measurements for gravity wave studies, *J. Geophys. Res.*, *114*, D07105, doi:10.1029/2008JD011241.

Jiang, J. H., D. L. Wu, and S. D. Eckermann (2002), Upper Atmosphere Research Satellite (UARS) MLS observation of mountain waves over the Andes, *J. Geophys. Res.*, *107*(D20), 8273, doi:10.1029/2002JD002091.

Lott, F., and M. J. Miller (1997), A new subgrid-scale orographic drag parameterization: Its formulation and testing, *Q. J. R. Meteorol. Soc.*, *123*, 101–127.

Orr, A., P. Bechtold, J. Scinocca, M. Ern, and M. Janiskova (2010), Improved middle atmosphere climate and forecasts in the ECMWF model through a nonorographic gravity wave drag parameterization, *J. Clim.*, *23*, 5905–5926, doi:10.1175/2010JCLI3490.1.

Perlwitz, J., S. Pawson, R. L. Fogt, J. E. Nielsen, and W. D. Neff (2008), Impact of stratospheric ozone hole recovery on Antarctic climate, *Geophys. Res. Lett.*, *35*, L08714, doi:10.1029/2008GL033317.

Preusse, P., A. Dörnbrack, S. D. Eckermann, M. Riese, B. Schaeler, J. T. Bacmeister, D. Broutman, and K. U. Grossmann (2002), Space based measurements of stratospheric mountain waves by CRISTA: 1. Sensitivity, analysis method and a case study, *J. Geophys. Res.*, *107*(D23), 8178, doi:10.1029/2001JD000699.

Sato, K., S. Tateno, S. Watanabe, and Y. Kawatani (2011), Gravity wave characteristics in the Southern Hemisphere revealed by a high-resolution middle-atmosphere general circulation model, *J. Atmos. Sci.*, in press.

Schmidt, G., et al. (2006), Present day atmospheric simulations using GISS Model E: Comparison to in-situ, satellite and reanalysis data, *J. Clim.*, *19*, 153–192.

Schoeberl, M. R., et al. (2004), Earth Observing System missions benefit atmospheric research, *Eos Trans. AGU*, *85*(18), 177.

Shutts, G. J., and S. B. Vosper (2011), Stratospheric gravity waves revealed in NWP model forecasts, *Q. J. R. Meteorol. Soc.*, *137*, 303–317.

Skamarock, W. C., J. B. Klemp, J. Dudhia, D. O. Gill, D. M. Barker, W. Wang, and J. G. Powers (2005), A description of the Advanced Research WRF version 2, *NCAR/TN-468+STR*, Natl. Cent. for Atmos. Res., Boulder, Colo.

Son, S.-W., et al. (2008), The impact of stratospheric ozone recovery on the Southern Hemisphere westerly jet, *Science*, *320*, 1486–1489.

Thompson, G., R. M. Rasmussen, and K. Manning (2004), Explicit forecasts of winter precipitation using an improved bulk microphysics scheme. Part I: Description and sensitivity analysis, *Mon. Weather Rev.*, *132*, 519–542.

Turner, J., J. C. Comiso, G. J. Marshall, T. A. Lachlan-Cope, T. Bracegirdle, T. Maksym, M. P. Meredith, Z. Wang, and A. Orr (2009), Non-annular atmospheric circulation change induced by stratospheric ozone depletion and its role in the recent increase of Antarctic sea ice extent, *Geophys. Res. Lett.*, *36*, L08502, doi:10.1029/2009GL037524.

Wells, H., S. B. Vosper, and X. Yan (2011), An assessment of a mountain-wave parameterization schema using satellite observations of stratospheric gravity waves, *Q. J. R. Meteorol. Soc.*, *137*, 819–828.

Wu, D. L., and S. D. Eckermann (2008), Global gravity wave variances from Aura MLS: Characteristics and interpretation, *J. Atmos. Sci.*, *65*, 3695–3718, doi:10.1175/2008JAS2489.1.

Wu, D. L., and J. W. Waters (1996), Satellite observations of atmospheric variances: A possible indication of gravity waves, *Geophys. Res. Lett.*, *23*(24), 3631–3634.

M. J. Alexander, NorthWest Research Associates, 3380 Mitchell Lane, Boulder, CO 80301, USA. (alexand@cora.nwra.com)

H. Teitelbaum, Laboratoire de Meteorologie Dynamique/E.N.S., 24 rue Lhomond, F-75235 Paris CEDEX 05, France.